




Atomic-scale study of compositional and structural evolution of early-stage grain boundary precipitation in Al–Cu alloys through phase-field crystal simulation

X. Shuai¹, Z. J. Wang², H. Mao¹, S. Tang^{3,*} , Y. Kong^{1,*}, and Y. Du¹

¹ State Key Lab for Powder Metallurgy, Central South University, Changsha 410083, Hunan, China

² State Key Laboratory of Solidification Processing, Northwestern Polytechnical University, Youyi Western Road 127, Xi'an 710072, China

³ National Key Laboratory of Science and Technology on High-Strength Structural Materials, Central South University, Changsha 410083, China

Received: 29 October 2020

Accepted: 30 March 2021

Published online:
10 May 2021

© The Author(s), under exclusive licence to Springer Science+Business Media, LLC, part of Springer Nature 2021

ABSTRACT

Interfacial solute clustering is an essential step preceding grain boundary (GB) precipitation. Both states, i.e., clusters and precipitates, alter the mechanical, chemical, and corrosion properties of materials. Continuum models cannot capture the atomic details of these phenomena, specifically of the transition from clustering to precipitation. We thus use the structural phase-field crystal (XPFC) model to study the compositional and structural evolution during GB clustering in Al–Cu alloys. The results show that the compositional evolution is dominated by solute segregation to lattice defects at the very beginning and then by confined spinodal decomposition along the GBs. The latter leads to a steep increase in the concentration and then the formation of disordered clusters. This structure acts as a precursor for phase nucleation, just like the decomposed solid solution, and Guinier–Preston zones are the precursors of the thermodynamically stable Al₂Cu phase in the interior of grains. Two modes of spinodal decomposition are found. (a) On low-angle tilt GBs, spinodal decomposition occurs at the dislocations that constitute the GB. (b) On high-angle tilt GBs, spinodal decomposition takes place inside the entire GB plane. In either case, the structural transition from the disordered low-dimensional precursor states to an ordered phase state takes place following the compositional enrichment. These results shed light on atomic-scale early-stage GB decomposition and precipitation processes in Al–Cu alloys and enrich our knowledge about the coupling effects between compositional and structural evolution during GB phase transformation phenomena.

Handling Editor: Avinash Dongare.

Address correspondence to E-mail: s.tang@csu.edu.cn; yikong@csu.edu.cn

Introduction

In the early stage of precipitation, supersaturated solid solution decomposes into a depleting solid solution matrix and clusters of solute atoms. This process is referred to as solute clustering and is a crucial step for the formation of second phase precipitates [1, 2]. Solute clustering influences the composition, structure, size, morphology, and dispersion of precipitates. Such characteristics can be employed to strengthen alloys, especially precipitation-hardening alloys [3, 4]. Generally, solute clustering occurs in the bulk of grains and at lattice defects such as dislocations [5–7] and grain boundaries (GBs) of polycrystalline alloys [8, 9]. It is well known that a GB is less coherent and more disordered compared to grain interiors. The structural disturbance translates to an interfacial excess free energy, referred to as GB energy. Driven by the decrease in the GB energy, solute atoms tend to segregate to GBs in multi-component alloys, as expressed for the mean-field case by the Gibbs adsorption isotherm [10]. The solute enrichment at GBs marks a state of chemical partitioning between GBs and the bulk. This affects the nucleation and growth of precipitates [11, 12], qualifying GB clustering as a more complex phenomenon compared to precipitation kinetics, precipitate morphology, and distribution inside the bulk [13].

GB clustering often proceeds through a sequence of evolution steps in terms of composition and microstructure. Nevertheless, there is no clear theoretical understanding of the transition from the oversaturated solute state to interfacial enrichment, decomposition, and precipitates. Prior to precipitation, the solute concentration increases at the GB through equilibrium (or non-equilibrium) segregation. While the classical Gibbs isotherm assumes GB segregation without chemical interactions, i.e., a perfect regular solution of the segregating component at the interface, the isotherm formulation of Hart and Guttman [14] also considers chemical interactions among the segregated species. Such solute effects imply the possibility of chemical decomposition and phase transformation phenomena, similar to known from bulk phase diagrams at the interfaces [7, 15]. This can, for instance, lead to the formation of low-dimensional spinodal decomposition phenomena at GBs, such as recently reported for aluminum alloys [16], steel [17–20], and high entropy alloys [21].

Compared with the precipitation in the bulk where the system may be even outside of a spinodal state (compared to the GB region), the Gibbs decoration of the defects and the high atomic mobilities in interfaces can promote (for instance, in Al–Cu alloys) formation of Cu enrichment and a confined spinodal decomposition [16]. Such low-dimensional spinodal decomposition at GBs renders the distribution of the interface composition inhomogeneous, thus affecting the nucleation of GB precipitates [22]. This implies that the high solute enrichment and associated low-dimensional compositional patterning along GBs are, in some cases, not merely due to statistical solute segregation but to planar spinodal decomposition [7, 15, 19, 23]. The spinodal decomposition may also lead to precursor states that precede and trigger structural transitions, e.g., the emergence of disordered states which acts as precursor states for GB precipitation [24–26]. Therefore, understanding of the compositional and structural evolution in GBs is crucial to understand the physical mechanisms of segregation, low-dimensional spinodal decomposition and solute clustering.

It is also essential to clarify the correlation between GB structure and such GB chemistry effects. GBs provide preferred nucleation sites through the structural disorder and associated interfacial energy, enabling heterogeneous nucleation [27–29]. Intergranular structures can significantly affect the compositional and structural evolution of clusters that form on GBs. Unwin and Nicholson [17] have proven experimentally that the nucleation and growth of GB precipitates in Al alloys are strongly affected by the structure of the interfaces. Regarding GB precipitation in Al–Zn and Al–Zn–Mg alloys, Gronsky and Furrer [30] found that individual dislocations act as nucleation sites for precipitation at low-angle tilt GBs. This resulted in a regular distribution of precipitates along with the low-angle tilt GBs, while precipitates at high-angle tilt GBs distributed less regularly. Also, the phase constitution and growth modes for GB precipitations vary with the type of GB [31–33]. These phenomena demonstrate the profound influences of GB structure on segregation, clustering, decomposition, and structural transformation. Yet, we still lack a clear theoretical understanding of the inter-dependence of composition and structure at GBs regarding these decomposition and phase formation phenomena.

This is due to challenges in modeling and electronic microscopy characterization of such phenomena, which must map several length scales on the one hand and both structure and chemistry on the other hand [34]. Purely continuum models such as the phase-field method are unable to depict atomistic details of such compositional and structural evolutions [35, 36]. Molecular dynamics (MD) and Monte Carlo (MC) simulations have been used to study phase transitions in GBs [37, 38], but both are less suited to simulate processes at diffusive time scales, such as required for understanding nucleation and growth at GBs. Recently, hybrid MC and MD atomistic simulations have been conducted to study linear complexions at dislocations [39, 40], yet, with limitations regarding the full dynamical resolution of the preceding solute partition and the structural transformations. Diffusive molecular dynamics (DMD) simulations of segregation and precipitation phenomena in an Al–Mg binary alloy by Dontsova et al. have the advantage of retaining atomistic details while allowing for the treatment of diffusive time scales [41, 42]. However, DMD faces challenges when simulating multi-component systems because of the limitations in describing solute concentrations for more than two elements [43].

Here, we employ the structural phase-field crystal model (also termed as XPFC) [44, 45] to simulate the process of solute enrichment and nucleation of GB precipitates, as this methodology can investigate materials processes over diffusive time scales, yet, at a near-atomic-scale resolution [44, 46, 47]. XPFC simulations have been successfully used to study materials processes such as crystal nucleation and growth, precipitation at dislocations, crystal defect dynamics, and microstructure evolution during deformation [44, 46, 48, 49].

In this work, we investigate the solute clustering phenomenon during the early stage of GB precipitation by using the XPFC model for the binary alloy. We focus on the correlation between GB structure and GB clustering, as well as the mechanisms of compositional and structural evolution during GB clustering. This paper is organized by introducing the XPFC model of Al–Cu binary alloy firstly and constructing the eutectic XPFC phase diagram for Al–Cu alloy. Additionally, we analyze the relationship between GB energy and GB structures by changing the misorientation and GB plane inclination. Further, we describe the compositional and structural

evolution during solute clustering at various GBs and analyze the effects of intergranular structure on the nucleation and growth of GB clusters. Finally, we uncover the interaction between compositional evolution and structural transformation during the process of GB clustering.

Method

The XPFC model for a binary Al–Cu alloy

The free energy functional of the XPFC model for binary alloy system is written as follows [49],

$$\frac{\Delta F}{kT\rho^0} = \int \left\{ \frac{n^2}{2} - \eta \frac{n^3}{6} + \chi \frac{n^4}{12} + (n+1)\Delta F_{\text{mix}} - \frac{1}{2}n \int dr' C_{\text{eff}}^n(|r-r'|)n' + \alpha |\nabla c|^2 \right\} dr \quad (1)$$

where ρ^0 is the atom number density of the reference state, n the reduced dimensionless atomic number density defined by $n = \rho/\rho^0 - 1$, $c = \rho_B/\rho$ represents the solute concentration field (ρ_B the number density of solute B), k is the Boltzmann constant, T is the temperature, η and χ are parameters introduced to fit the ideal energy with a polynomial expansion, and

$$\Delta F_{\text{mix}} = \omega \left\{ c \ln\left(\frac{c}{c_0}\right) + (1-c) \ln\left(\frac{1-c}{1-c_0}\right) \right\} \quad (2)$$

where ΔF_{mix} denotes the entropy of mixing. The coefficient ω is introduced to correct the entropy of mixing away from the reference composition c_0 . The gradient energy coefficient α sets the scale and energy of compositional interfaces ($\alpha = 1$ in this paper) [47].

In the XPFC model for binary alloys system [45], the effective correlation function C_{eff}^n describes the interaction between atoms and thus contributes to excess energy that includes crystalline symmetry and elasticity in the system. In the XPFC model, it shapes the stability of the crystal structure and topological defects such as dislocations and GBs, and is written as

$$C_{\text{eff}}^n = X_1(c)C_2^{\text{AA}} + X_2(c)C_2^{\text{BB}} \quad (3)$$

where

$$\begin{aligned} X_1(c) &= 1 - 3c^2 + 2c^3 \\ X_2(c) &= 1 - 3(1-c)^2 + 2(1-c)^3 \end{aligned} \quad (4)$$

are interpolation functions associated with the two direct correlation functions C_2^{AA} and C_2^{BB} , which interpolate between direct correlation functions of the pure species, weighting each by the local compositions [50]. These direct correlation functions assume only inter-particle interactions, temporally averaged over all particles. In Fourier space, they are written as,

$$\hat{C}_2^{ii} = \sum_j \hat{C}_{2j}^{ii} = \sum_j e^{-\frac{\sigma^2}{\sigma_{Mj}^2}} e^{-\frac{(k-k_j)^2}{2\alpha_j^2}} \quad (5)$$

where $ii = AA$ and BB in the binary case, \hat{C}_{2j}^{ii} the j th reciprocal space peaks or Gaussian peaks at position k_j determined by each component’s equilibrium crystal unit cell structure. Each peak is represented by the width of the Gaussian peak α_j , modulated for temperature by Debye–Waller prefactor which accounts for the effective temperature σ and an effective transition temperature σ_{Mj} . The interface energy, elastic coefficients, and their anisotropy are determined by setting α_j appropriately [44, 51]. As demonstrated in Eq. (5), the direct correlation function \hat{C}_2^{ii} is the envelope of all peaks \hat{C}_{2j}^{ii} included to represent the atomic interactions. The total atomic density is defined as the summation of the density of each component ($\rho = \rho_A + \rho_B$, $\rho^o = \rho_A^o + \rho_B^o$), that of liquid at solid–liquid coexistence. The dynamic equation of motion can be written as

$$\frac{\partial n}{\partial t} = \vec{\nabla} \cdot \left\{ M_n \vec{\nabla} \left(\frac{\delta F}{\delta n} \right) \right\} \quad (6)$$

$$\frac{\partial c}{\partial t} = \vec{\nabla} \cdot \left\{ M_c \vec{\nabla} \left(\frac{\delta F}{\delta c} \right) \right\} \quad (7)$$

where t is the evolution time and M_n and M_c are the dimensionless kinetic mobility parameters. In the study, the mobility coefficients are considered as constants at a given temperature (i.e., equal to 1 for all mobilities) [52]. These dynamic equations in the XPFC methodology are similar to traditional phase-field methods in terms of the representation of mass as a continuous density field and a concentration field evolving at diffusive time scales. Moreover, it goes beyond a phase-field description by capturing atomic-scale details of systems.

Results and discussion

Computation of the Al–Cu phase diagram and simulation details

We focus on the transformation from an Al–Cu solid solution (fcc-A1) into a decomposed mixture of an Al–Cu solid solution and the precipitated phase Al_2Cu . for all solid phases, the widths of the correlations peaks are taken $\alpha_{111} = 0.8$ and $\alpha_{100} = \sqrt{3}/2\alpha_{111}$. The primary vectors in the reciprocal lattice of pure Al and θ - Al_2Cu phase $k_{111Al} = 2\pi$, $k_{100Al} = 2/\sqrt{3}k_{111Al}$, $k_{111\theta} = (81/38)\pi$, $k_{100\theta} = 2/\sqrt{3}k_{111\theta}$ [52]. Though some atomistic scale information is smeared by this simplicity, the square lattice could at least roughly reveal some atomic information such as dislocation, GB structures, and fcc-A1/ θ - Al_2Cu interface structure in the direction of $\langle 001 \rangle$ orientation. The initial condition of the XPFC simulation is determined by the effective temperature σ and the system’s average composition \bar{c} . Both are chosen based on the XPFC eutectic phase diagram of a binary Al–Cu alloy with respect to σ and \bar{c} . The phase diagram is calculated as follows. Firstly, we employ the dynamic equations to equilibrate the phases placed in the simulation box. The free energy curves of the solid phases are calculated using a two-mode approximation of the density fields [52], as shown in Fig. 1a, b. Secondly, by fixing σ to constants spanning from 0 to 0.5, we obtain the free energy curves of effective temperature. The coexistence lines between the respective phases are obtained by constructing the common tangents to the free energy curves of solid and liquid phases at the reference density. Finally, the XPFC eutectic phase diagram in Fig. 1 is constructed by connecting coexisting regions for various values of σ .

The obtained eutectic phase diagram agrees well with the Al-rich side of the experimentally observed Al–Cu phase diagram [53], which describes the relationship between fcc-Al and the intermetallic phase Al_2Cu (containing ≈ 32.5 at% Cu [54]). Based on this phase diagram, the initial concentration \bar{c} of the supersaturated Al–Cu solid solution is set as 4.5%, and the quenched temperature $\sigma = 0.05$ in all the simulations in this work. There are two steps about

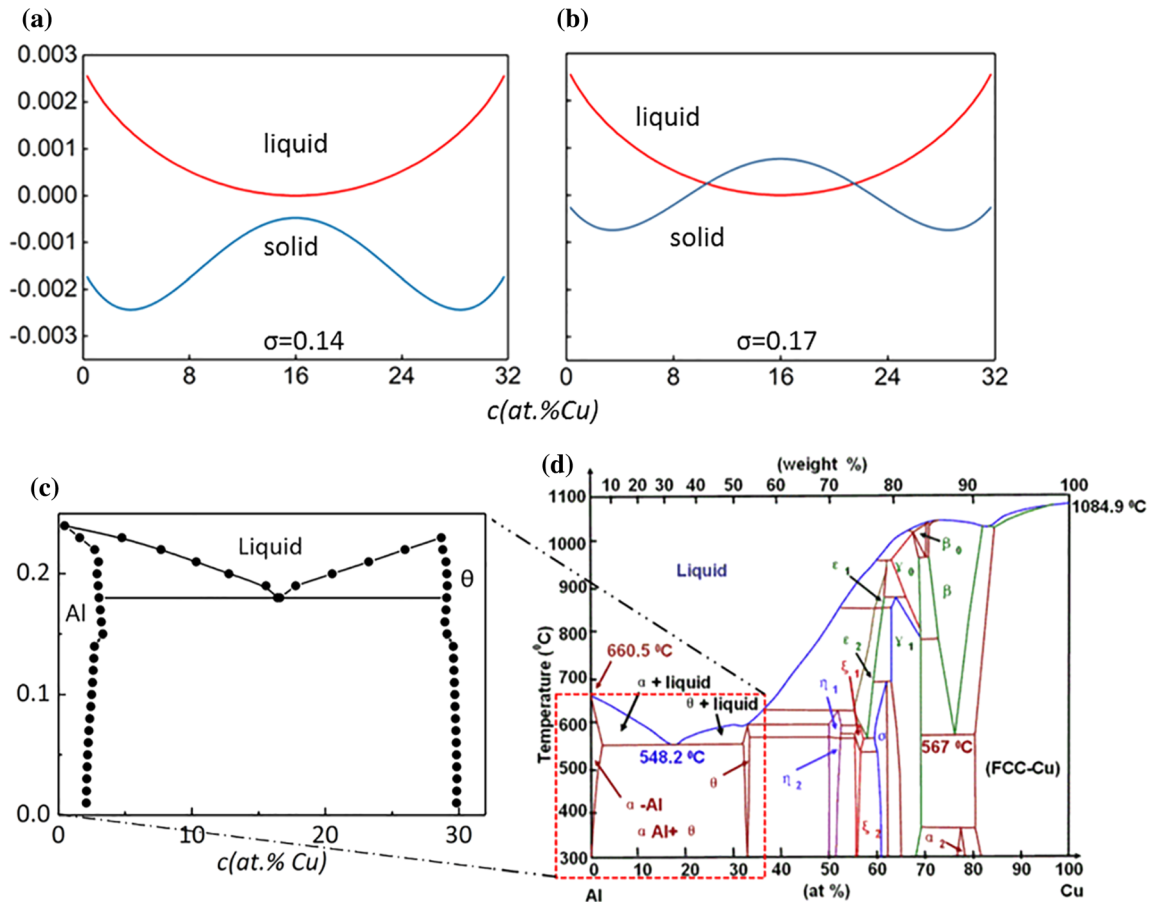


Figure 1 Phase diagram. **a–b** Solid and liquid energy curves at different temperatures calculated using XPFC mode approximation. **c** Eutectic phase diagram for a binary Al–Cu alloy in the frame of the present XPFC model. **d** the experimental

phase diagram of the Al–Cu system taken from Ref. [53]. The polynomial fitting parameters were $\eta = 1.4$, $\chi = 1$ and $\omega = 0.005$, while XPFC parameters $\sigma_{Mi} = 0.6$, $\alpha_i = 0.8$, and the reference composition $c_0 = 0.5$.

the setting of the initial condition. Firstly, we initially place two abutting crystals, separated by a liquid film with a width of roughly 10 grid points. The purpose of the introduction of the liquid film is to give rise into a relaxed GB. Then we start the simulation; the liquid film disappears soon and is replaced by the GB we need. Secondly, we reset the initial value of the composition of the whole simulation box and restart the simulation of GB clustering. Figure 2 shows the orientation of the two grains is determined based on the two angles θ and ϕ , which are the GB misorientation angle and GB plane's orientation angle, respectively. The size of the simulation box is set as $3840\Delta x \times 3840\Delta x$ (480×480 atoms). Grid spacing $\Delta x = 0.125$, and time step $\Delta t = 0.1$ (the value of parameters shown on the Table 1).

The correlation between GB structure and GB clustering

GB clustering processes at various GBs

Figure 2 describes the formation of solute clusters at various GBs of the Al–Cu binary alloy system. We compare GB clustering in low-angle tilt GBs ($\theta = 4^\circ$) with that in high-angle tilt GBs ($\theta = 36.5^\circ$), and GB clustering in symmetric ($\phi = 0^\circ$) with that in asymmetric tilt GBs ($\phi = 5^\circ$). The GB cluster formation processes go through four steps: (a) solute enrichment in the GBs, (b) the nucleation of clusters, (c) the growth of clusters, and (d) coarsening and merging of clusters.

The solute enrichment proceeds through GB solute segregation and compositional spinodal decomposition in GBs. Figure 2 a, e shows that solute

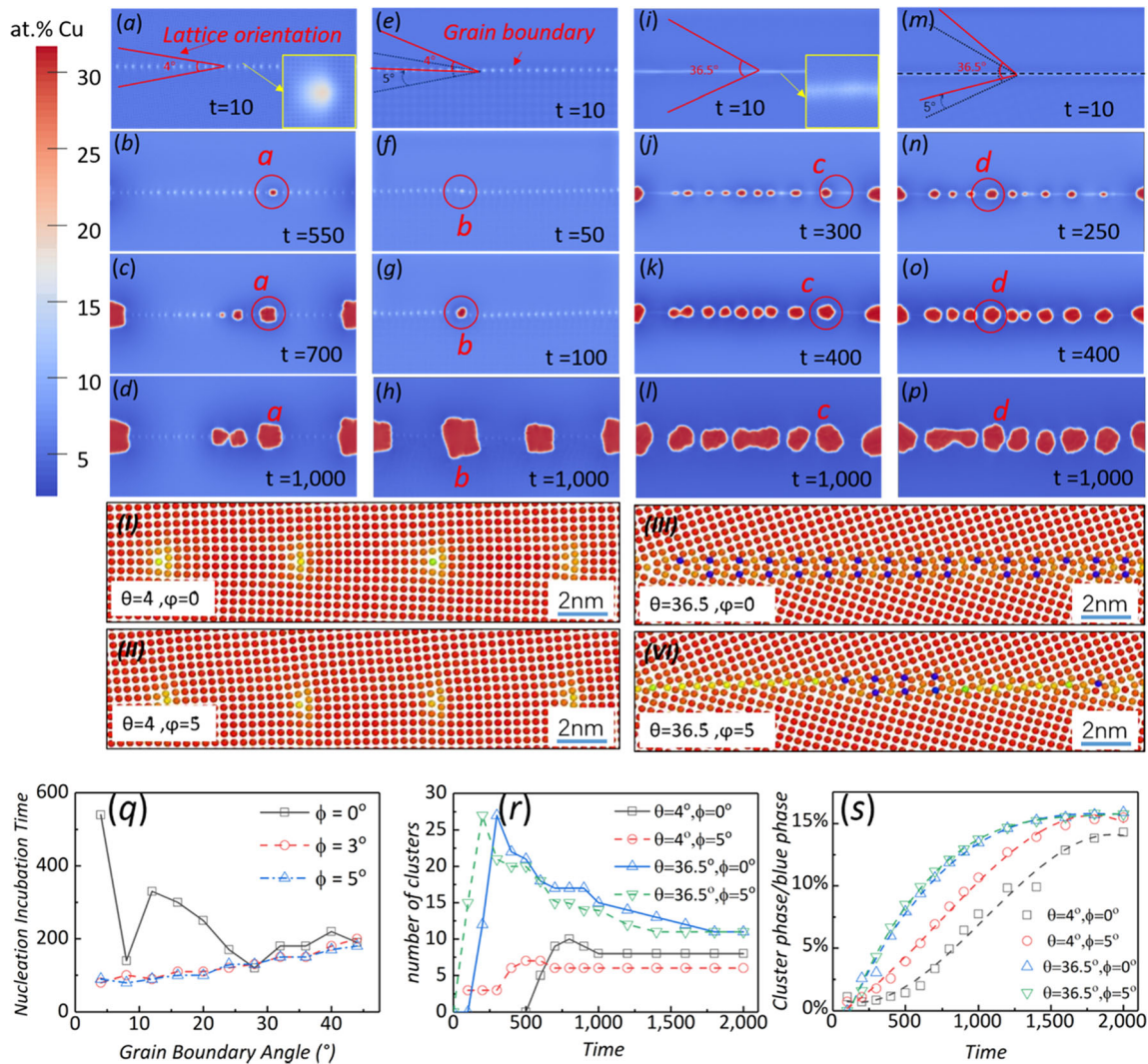


Figure 2 GB clustering processes. **a–d** GB misorientation angle $\theta = 4^\circ$, GB plane orientation $\phi = 0^\circ$; **e–h** $\theta = 4^\circ$, $\phi = 5^\circ$; **i–l** $\theta = 36.5^\circ$, $\phi = 0^\circ$; **m–p** $\theta = 36.5^\circ$, $\phi = 5^\circ$. The red circles and labels a-d indicate precipitations in these four types of grain boundaries. The atomic configurations of the four GBs are shown in the inset figures I–IV respectively. The color is rendered only for the characterization of the GB structures. **q** incubation time of

nucleation as a function of θ and ϕ ; **r** number of clusters as a function of time for different GBs; **s** the phase fraction of precipitated phase as a function of time for different GBs. Note that the atomic-scale information in **a–p** is smeared due to the over the reduction of images' size (for atomic-scale information, please refer to the zoomed-in images in Figs. 3 and 4).

Table 1 Parameters used in PFC simulation about the GB clustering of Al–Cu alloy

Parameters	Symbols	Values/expressions
Reference density	ρ^0	0.01
Reference composition	c_0	0.5
Polynomial fitting parameters	η, χ	$\eta = 1.4, \chi = 1$
Entropy of mixing coefficient	ω	0.005
XPCF parameters	σ_{Mi}, α_i	$\sigma_{Mi} = 0.6, \alpha_i = 0.8$
Gradient energy coefficient	α	1
Grid spacing	Δx	0.125*lattice constant

r_0 the average atomic spacing (matrix phase)

segregation to GBs occurs initially. Then, the increase in Cu concentration around the dislocation (via the uphill diffusion) triggers spinodal decomposition in GBs. This process can be characterized on an atomic-scale by local compositional variations confined to several intergranular dislocations in Fig. 3a, b. It is observed that these compositional variations have become increasingly drastic with time. The concentration profiles denoted by yellow lines in the right panels of Fig. 3 indicate that the local compositional variations pattern is quantified by an average

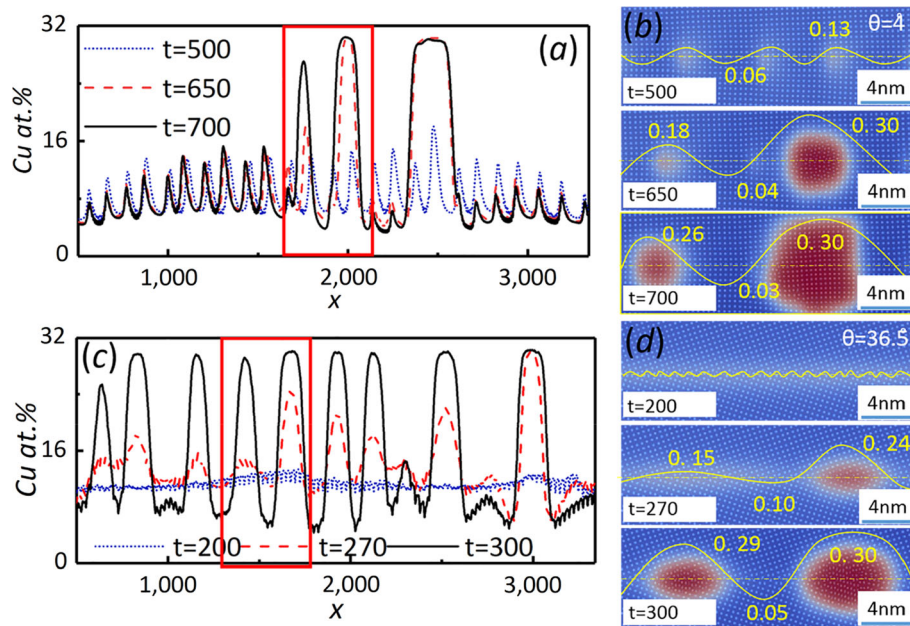


Figure 3 The time evolution of concentration profiles along symmetrical GBs. **a** Low-angle tilt GB, **b** the evolution of the morphology of low-angle tilt GB cluster formation, **c** high-angle tilt GB, **d** the evolution of the morphology of high-angle tilt GB

concentration of about 10 at% Cu as well as by fluctuations ranging between 3 and 30 at% Cu. Then, the nucleation of the GB cluster occurs at the peaks of composition fluctuations. In contrast, we observe another spinodal decomposition behavior in the high-angle tilt GBs in Fig. 3c, d. Compositional variations distribute along with the entire high-angle tilt GBs uniformly rather than on several preferred positions (e.g., dislocations in low-angle tilt GBs). Figure 3c, d shows that the segregation of Cu to the high-angle tilt GB contributes to an average concentration of about 10 at% Cu. Then GB spinodal decomposition proceeds and leads to a bunch of uniformly distributed compositional variations ranging between 5 and 30 at% Cu. Similar compositional variations have been termed as low-dimensional spinodal decomposition in recent experimental studies [55–58]. Our results indicate that the spinodal decomposition in low-angle tilt GB differs from that in high-angle tilt GB in terms of the range of fluctuations along GBs.

Such GB spinodal decomposition processes can be explained in the frame of the GB complex theory. The concept of GB complex was invented in recent years to explain the phase-like behaviors of GBs [40]. For instance, GB structure, chemistry, and properties

cluster formation. Yellow solid lines in the right panels are concentration profiles along the GBs (marked by dashed yellow lines).

may change discontinuously at critical points of thermodynamic status [59]. It is regarded GBs may undergo a phase transformation as an ordinary phase does base on the theory of GB complexes [60]. In our simulations, the chemical composition of GBs is initially altered by solute segregation to GBs. Then GB spinodal decomposition greatly promotes solute transportation along GBs. This leads to the onset of the nucleation of the solute cluster as the concentration of the peaks of composition fluctuations reaches a critical value (of about 30 at% Cu).

In the nucleation step, we find the nucleation behavior depends strongly on the GB structure. Figure 2b presents that the nucleus appears firstly around the dislocation due to local spinodal decomposition in low-angle tilt GB. Being interesting, the nucleation in high-angle tilt GB is very different. It occurs at the peaks of the concentration profile. These peaks are distributed periodically along with the entire GB instead of being merely confined to dislocations. This leads to the emergence of a bunch of clusters simultaneously. Thus, we find an abrupt increase of cluster number during the nucleation of GB clustering in Fig. 2j, n, r. Furthermore, the kinetics of nucleation, such as incubation time and nucleus number, is affected by the misorientation angle (θ) of

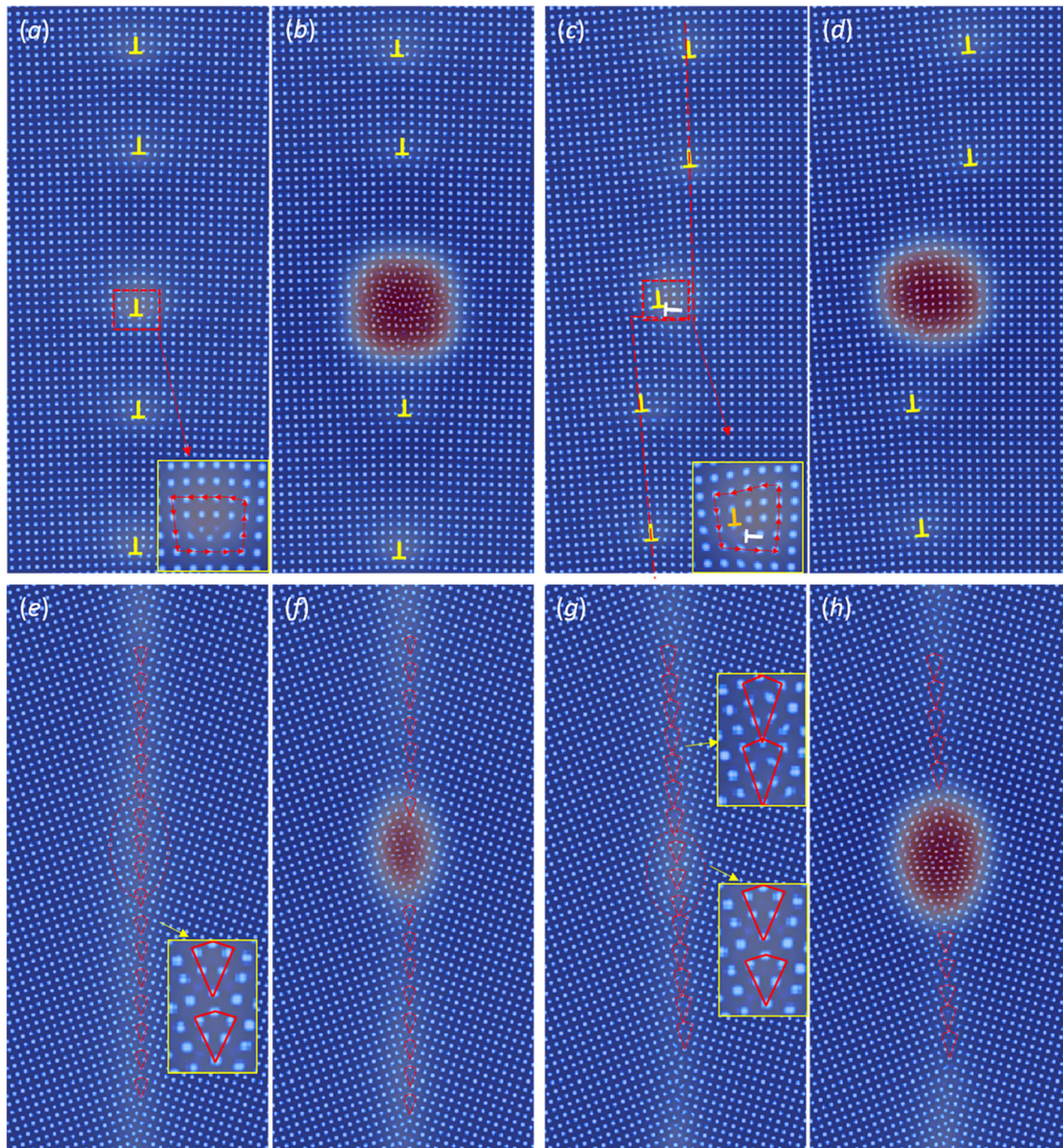


Figure 4 Microstructure evolution of nucleation sites at GBs. (**a, b**) GB misorientation angle $\theta = 4^\circ$, GB plane orientation $\phi = 0^\circ$; (**c, d**) $\theta = 4^\circ$, $\phi = 5^\circ$; (**e, f**) $\theta = 36.5^\circ$, $\phi = 0^\circ$; (**g, h**) $\theta = 36.5^\circ$, $\phi = 5^\circ$.

GB and orientation (ϕ) of the GB plane. Figure 2q indicates that a small rotation of the GB plane substantially shortens the incubation time for low-angle tilt GB while exerts limited influence on the incubation time for high-angle tilt GB. The time evolution of the cluster number is shown in Fig. 2r. We can see that cluster number shows strong dependences on θ , while little on ϕ .

As to the growth and coarsening stages of GB clustering, the average size of clusters on low-angle

tilt GBs is larger than that on high-angle tilt GBs. Low-angle tilt GBs have fewer clusters competing for feeding atoms than high-angle tilt GBs. Moreover, Fig. 2s shows that the fractions of the precipitated phase in these GBs gradually converge over time. Also, we find that a small rotation of the GB plane accelerates the growth of clusters in low-angle tilt GBs substantially, while exerts little influence on the growth of clusters in high-angle tilt GB. When comparing the cluster morphology in low-angle GB in

Figs. 3b and 2h with that in high-angle tilt GB in Figs. 3d and 2l, the clusters in the low-angle tilt GB are discrete and present nearly square shape, while those in the high-angle tilt GB are connected and present ellipsoidal shape. Sandeep Sahu found semi-continuous and continuous shapes in the early stage of precipitation in random high-angle tilt GBs, while discrete precipitates in low-angle tilt GBs [61]. This is in line with our simulations qualitatively.

The influence of intergranular structure on the nucleation of clusters

The nucleation sites of cluster nucleation on the symmetric and asymmetric low-angle tilt GB are shown in Fig. 4. In the symmetrical low-angle tilt GB, the clusters are mainly nucleated near the edge dislocations, as mentioned above. When the low-angle tilt GB plane rotates by 5° , a small step formed in the tilt GB. This small step is composed of two mutually perpendicular dislocations. It has a stronger adsorption capacity for the solute and thus can greatly promote the nucleation of clusters.

The symmetric high-angle tilt GB in Fig. 4a is constituted of a chain of structural units with a diamond shape. The structures of the nucleation site show little difference from those of the adjacent regions. For the asymmetric high-angle tilt GB, we observe the structural unit consisting of six atoms transforms into a structural unit with eight atoms. Figure 2q–s presents that differences among GB structures affect the strength of spinodal decomposition and make the nucleation kinetics different from that of the corresponding symmetric high-angle tilt GB.

The dependence of work of formation of nucleation on GB structure

The energy barrier of nucleation also changes with GB structure. The total work of cluster nucleation is calculated in the way proposed by Fallan et al. [52]. Figure 5 shows the total work of formation initially increases with the size of the embryo and then decreases when the embryo reaches its critical radius. We find that the work of formation and critical radius of the nucleus changes substantially with GB structure. The total work of formation during the process of clustering on high-angle tilt GB is lower than that of low-angle tilt GB, resulting in a smaller critical

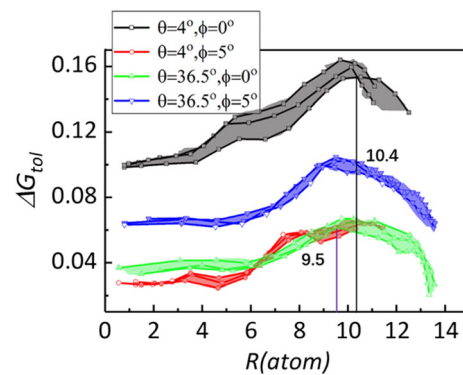


Figure 5 Total work of formation ΔG_{tot} for nucleation of clusters versus cluster size R in various GBs. Note that to ensure the reliability of data, three nuclei are investigated in each GB.

radius for nucleation (about 10.4 atoms for low-angle tilt GB and 9.5 atoms for high-angle tilt GB). In the case of low-angle tilt GB, the rotation of GB can significantly reduce the total work of formation. The reasons behind this are the destruction of symmetrical structures and the formation of the small step in Fig. 4c. On the contrary, the rotation of the high-angle tilt GB increases the work of formation. It can be observed in Fig. 4e, g the variations of structural units at the nucleation site in the high-angle tilt GB due to the rotation of the GB plane, e.g., the transition from the original six-atom structure unit A to eight-atom structure unit B. However, cluster nucleation occurs more easily at structure unit A, implying that the formation of the structure unit B leads to the increase of work of formation. This may be the reason that leads to the opposite trends of the low-angle and the high-angle tilt GBs with respect to rotation.

Mechanisms of cluster formation in the early stage of GB precipitation

The formation of disordered intermediate precursor

As we mentioned above, the nucleation of the cluster is triggered by GB spinodal decomposition, which results in a steep increase in solute concentration at nucleation sites. Figure 6b— $t = 550$ and 6d— $t = 100$ shows that the disordered precursor is generated in the low-angle tilt GBs as the concentration rapidly increases to 30 at% Cu. Then, the disordered structure evolves into a stable structure. In the case of high-angle tilt GBs, due to the effect of spinodal decomposition, the peaks of concentration fluctuations firstly lead to the generation of disordered

Figure 6 Compositional and structural evolution of cluster formation processes in low-angle tilt GBs. **a** A symmetric low-angle tilt GB with misorientation angle $\theta = 4^\circ$ and GB plane orientation $\phi = 0^\circ$, **c** an asymmetric low-angle tilt GB with $\theta = 4^\circ$ and $\phi = 5^\circ$; **b** and **d** are atomic configurations of clusters corresponding to **a** and **c**, respectively. The red boxes represent the concentration distribution corresponding to the structure diagram on the right panels.

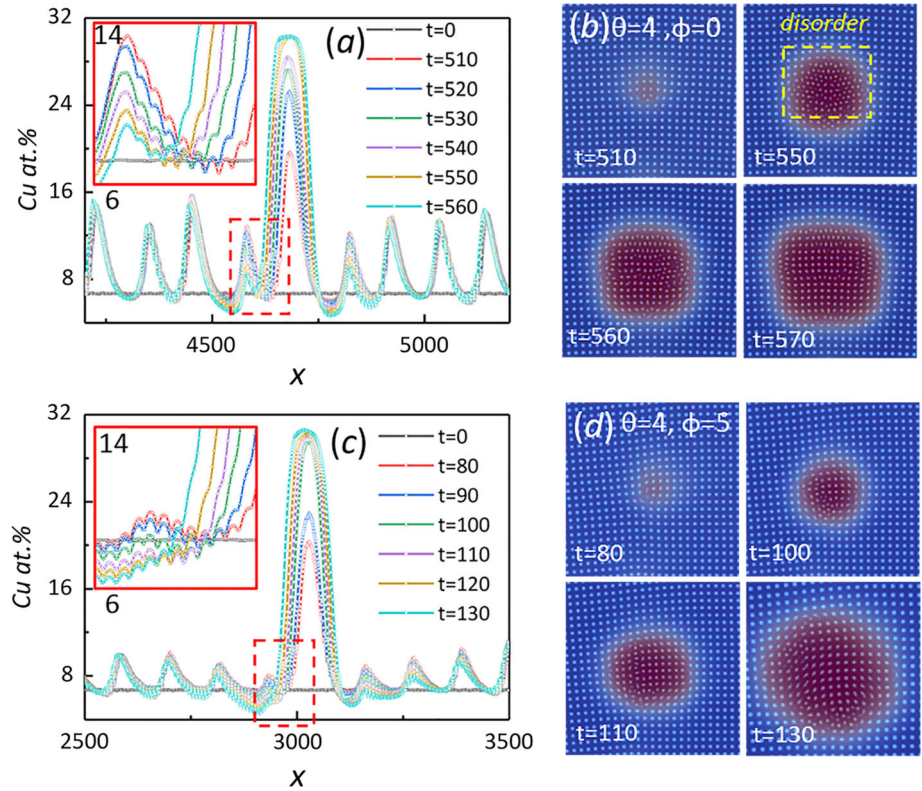
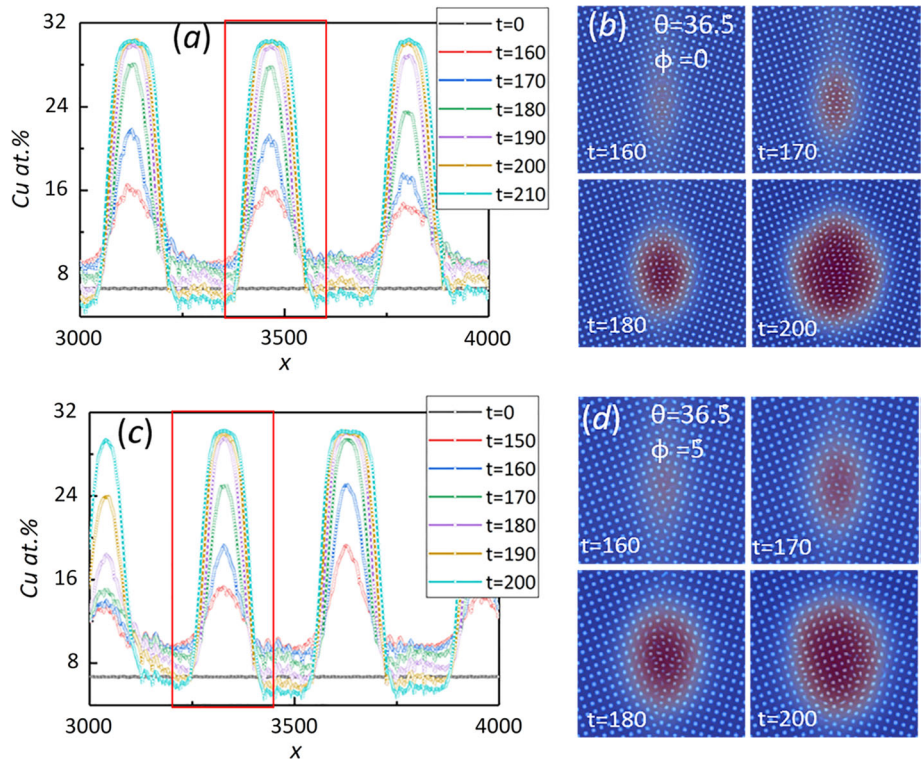


Figure 7 Compositional and structural evolution of cluster formation processes in high-angle tilt GBs. **a** A symmetric high-angle tilt GB with misorientation angle $\theta = 36.5^\circ$ and GB plane orientation $\phi = 0^\circ$, **c** an asymmetric high-angle tilt GB with $\theta = 36.5^\circ$ and $\phi = 5^\circ$; **b** and **d** are the atomic configuration of cluster corresponding to **a** and **c**, respectively. The red boxes represent the concentration distribution corresponding to the structure diagram on the right panels.



precursors (Fig. 7a— $t = 180$ and 7c— $t = 180$). These disorder clusters distribute periodically along with

the entire GB. Then, the new phase in Fig. 7b— $t = 200$ and 7d— $t = 200$ evolved from disordered

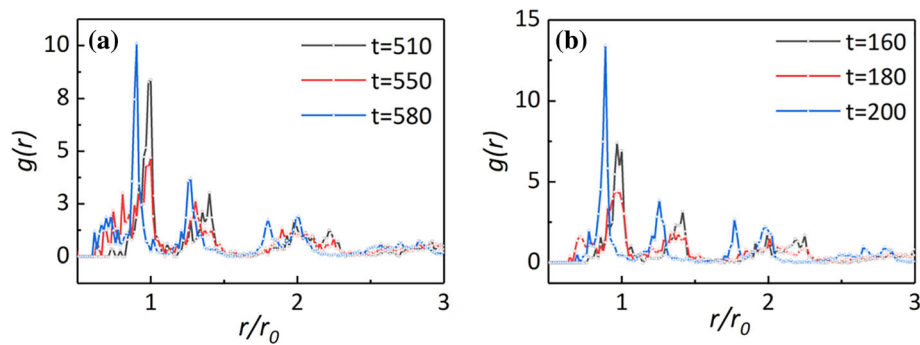


Figure 8 Radial distribution functions (RDFs) for nuclei during the clustering process. **a** Low-angle tilt GB with $\theta = 5^\circ$ and **b** high-angle tilt GB with $\theta = 36.5^\circ$. The black, red, and blue curves represent the RDFs of the matrix, intermediate disorder

precursor, and final stable new phase, respectively. The r/r_0 is the ratio of the average atomic spacing in the precipitation region to that in the matrix phase.

precursors grows toward both sides of the matrix phase. Such disordered structure is characterized by wide peaks in radial distribution functions (RDFs) (Fig. 8). Similar disorder clusters have also been observed in the transformation from the solid solution into final stable precipitates in aluminum alloys [62–65]. However, the formation process and underlying physics about the disorder clusters are still unclear, because it is still a formidable challenge to characterize their formation process on an atomic scale in real time. Our simulations help us to move this issue forward by illustrating that such disorder clusters are attributed to the GB spinodal decomposition of solid solution around nucleation sites and by systematically clarifying the correlation between GB structure and such disorder clusters.

The coupling effect between compositional evolution and structural evolution

Figure 9 presents in detail about the correlation between compositional and structural evolution. Black and red curves in Fig. 9a, b quantify the solute evolution of symmetrical low-angle and high-angle tilt GBs, respectively. The concentration enrichment curve near the nucleation sites in our simulations can be divided into a slow increase stage via solute segregation and a rapid increase stage through GB spinodal decomposition. We observe that the latter stage is triggered when the concentration increases to about 15 at% Cu by solute segregation. Particularly,

as mentioned above, the small step on the asymmetric low-angle tilt GBs greatly promotes the solute segregation. As a result, the solute content increases to the critical nucleation concentration (30 at% Cu) quickly.

The GB phase transformation is activated by the abrupt change of solute concentration via GB spinodal decomposition. Figure 9b presents the atomic configuration around the nucleation site versus concentration. In the first stage dominated by solute segregation, the lattice structure of the nucleation site in Fig. 9I, III changes little. In the second stage, as GB spinodal decomposition proceeds, variations of the ratio r/r_0 arise and reflect the lattice distortion around the nucleation site. The increase in solute concentration aggravates lattice distortion in the Al–Cu solid solution. Substantial lattice distortion leads to the decomposition of the solid solution and then the metastable disorder phase around the nucleation sites. After points II and IV, when the solute concentration increases to about 30%, the ratio r/r_0 begins to decrease steeply, corresponding to the transition from the disordered precursor into the final stable phase. Besides, the effect of lattice distortion in structural evolution is analogous to that of propagation of strains in the elastic–plastic deformation process. Here, the lattice distortion increases with solute concentration initially. Disordered clusters, as shown in Fig. 9II, IV, are formed when the increased lattice distortion exceeds the capacity of the cluster to accommodate misfit strain.

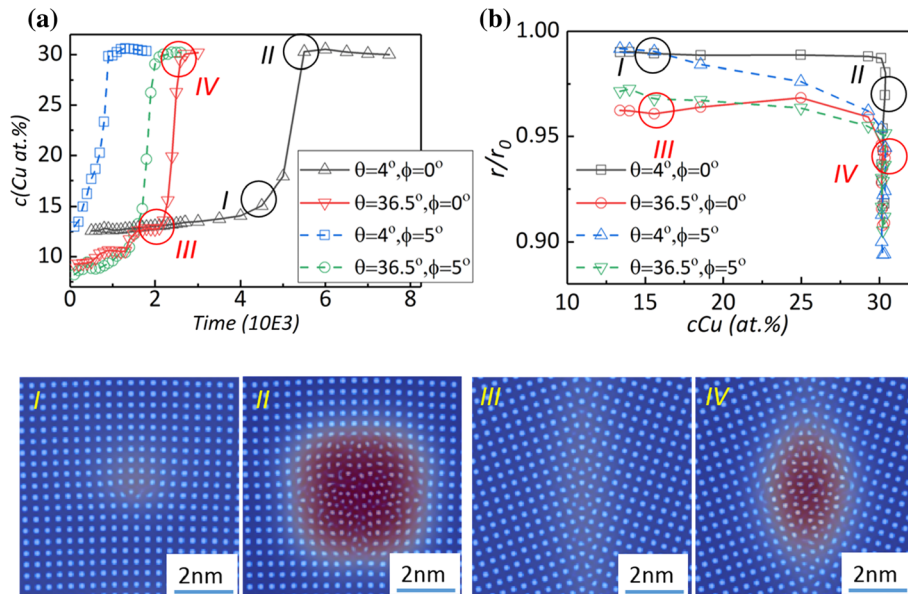


Figure 9 The coupling between compositional and structural evolution during cluster formation in GBs. **a** Compositional evolution of Cu at nucleation sites as a function of time and GB structure; **b** the change of the ratio of average cluster atomic spacing r to lattice constant of matrix phase ($a_{\text{matrix}} = 1$) as a function of the concentration of Cu (the r/r_0 is the ratio of the average atomic spacing in the precipitation region to that in the

matrix phase.) Inset figures (I) and (III) are, respectively, the atomic configurations around the nucleation site on the low-angle symmetric tilt GB before disorder appears (point I in (a) and (b)) and after disorder appears [point II in (a) and (b)]. Similarly, inset figures (III) and (IV) are the atomic configurations for the case of the high-angle symmetric tilt GB.

Conclusion

In this study, we employed the XPFC simulations to analyze the compositional and structural evolution of solute clustering during the early stage of GB precipitation in Al–Cu alloys. The main conclusions are as follows:

1. The nucleation of clustering in the early stage of GBs clustering undergoes three steps: (I) the first stage is the segregation of Cu to the GBs, driven by the Gibbs isotherm adsorption; (II) once Cu is enriched at the GBs, it does not behave like an ideal solid solution. However, it undergoes a GB local spinodal decomposition confined to the defects; (III) the maxima of the low-dimensional spinodal decomposition appear at the GBs and form first nuclei.
2. The influence of GB structure on cluster formation is clarified. We quantified that the nucleation barrier, nucleation site, and growth rate of the nucleated cluster depend closely on the misorientation of GBs and, in particular, the orientation of the GB plane of low-angle tilt GBs.

3. The coupling effect between compositional and structural evolutions is uncovered. The enrichment and transportation of solute concentration in GB are initially dominated by GB segregation and then by low-dimensional spinodal decomposition in GBs. The former results in a slow increase of Cu concentration, while the latter causes an abrupt increase in concentration and triggers the onset of structural transformation of clustering, e.g., the formation of disorder precursor due to abundant misfit strain caused by a steep increase of concentration.

These results have shed light on the poorly known microscopic mechanisms of chemical and structural evolution during the early stage of GB clustering. This work demonstrates that precipitation doesn't occur "randomly" at both low- and high-angle tilt GBs. Instead, nucleation sites distributed regularly along GBs are determined by the heterogeneities in intergranular structure and the inhomogeneous distribution of concentration along GBs. And not only that, the mechanism and kinetics of GB cluster nucleation and growth are also dominated by the coupling effect between the two factors.

Nevertheless, in the framework of the current XPFC model, it is still a great challenge to describe the overall picture of the structural transformations during GB precipitation. We need to construct a modified formulation of the correlation kernel for a new XPFC model that can describe the chemical and structural ordering of intermediate phases more clearly. Moreover, although the two-dimensional simulations in this work can qualitatively describe the thermodynamic forces and kinetics of precipitation as reported in previous studies, it is still needed to conduct three-dimensional simulations due to the fact that more intergranular structures and structurally assisted nucleation events can be captured.

Acknowledgements

This work was supported by grants from the National Natural Science Foundation of China (Grant Nos. 51531009, 51801237), and the fund of the State Key Laboratory of Solidification Processing in NWP (SKLSP201827).

Declarations

Conflict of interest The authors declare that they do not have any conflict of interest.

References

- Seidman DN, Marquis EA, Dunand DC (2002) Precipitation strengthening at ambient and elevated temperatures of heat-treatable Al(Sc) alloys. *Acta Mater* 50:4021. [https://doi.org/10.1016/S1359-6454\(02\)00201-X](https://doi.org/10.1016/S1359-6454(02)00201-X)
- Rambabu P, Prasad NE, Kutumbarao VV, Wanhill RJH (2017) Aluminium alloys for aerospace applications. *Aerospace materials and material technologies*, Springer
- Esmaili S, Wang X et al (2003) On the precipitation-hardening behavior of the Al–Mg–Si–Cu alloy AA6111. *Metall Mater Trans A* 34(13):751. <https://doi.org/10.1007/s11661-003-0110-4>
- Smallman RE, Ngan AHW (1963) Precipitation hardening. Pergamon
- Dong Q, Howells A, Lloyd DJ, Gallerneault M, Fallah V (2020) Effect of solidification cooling rate on kinetics of continuous/discontinuous Al₃(Sc, Zr) precipitation and the subsequent age-hardening response in cold-rolled AlMgSc(Zr) sheets. *Mater Sci Eng, A*. <https://doi.org/10.1016/j.msea.2019.138693>
- Wu L, Li Y, Li X, Ma N, Wang H (2020) Interactions between cadmium and multiple precipitates in an Al–Li–Cu alloy: improving aging kinetics and precipitation hardening. *J Mater Sci Technol* 46:44. <https://doi.org/10.1016/j.jmst.2019.11.032>
- Kwiatkowski A, da Silva D, Ponge ZP et al (2018) Phase nucleation through confined spinodal fluctuations at crystal defects evidenced in Fe–Mn alloys. *Nat Commun* 9:1137. <https://doi.org/10.1038/s41467-018-03591-4>
- Zhang J, Li HWG, Bozhilov K, Jin Z (2004) Faulting induced by precipitation of water at grain boundaries in hot subducting oceanic crust. *Nature* 428:633. <https://doi.org/10.1038/nature02475>
- L'Vov PE, Svetukhin VV (2018) Precipitation kinetics in binary alloys near grain boundaries. *Phys Solid State* 60:791. <https://doi.org/10.1134/S1063783418040200>
- Belton GR (1976) Langmuir adsorption, the gibbs adsorption isotherm, and interracial kinetics in liquid metal systems. *Metall Trans B* 7:35. <https://doi.org/10.1007/BF02652817>
- Lei Y, Ito Y, Browning ND, Mazanec TJ (2010) Segregation effects at grain boundaries in fluorite-structured ceramics. *J Am Ceram Soc* 85:2359. <https://doi.org/10.1111/j.1151-2916.2002.tb00460.x>
- Seah MP, Hondros ED (1973) Grain boundary segregation. *Proc R Soc Lond* 335:191. <https://doi.org/10.2307/2397194>
- Graux A, Cazottes S, De Castro D et al (2019) Precipitation and grain growth modelling in Ti–Nb microalloyed steels. *Materialia*. <https://doi.org/10.1016/j.mtla.2019.100233>
- Guttman AJ, Kim D, Thompson CJ (1977) Critical isotherm of Dyson's hierarchical model. *J Phys A Gen Phys* 10:L125. <https://doi.org/10.1088/0305-4470/10/6/007>
- Kwiatkowski A, da Silva G, Leyson MK et al (2017) Confined chemical and structural states at dislocations in Fe–9wt%Mn steels: a correlative TEM-atom probe study combined with multiscale modelling. *Acta Mater* 124:305. <https://doi.org/10.1016/j.actamat.2016.11.013>
- Zhao H, Frédéric DG, Alisson KdS et al (2018) Segregation assisted grain boundary precipitation in a model Al–Zn–Mg–Cu alloy. *Acta Mater*. <https://doi.org/10.1016/j.actamat.2018.07.003>
- Kwiatkowski da Silva RDKA, Ponge D, Gault B, Neugebauer J, Raabe D (2019) Thermodynamics of grain boundary segregation, interfacial spinodal and their relevance for nucleation during solid-solid phase transitions. *Acta Mater* 168:109. <https://doi.org/10.1016/j.actamat.2019.02.005>

- [18] Silva D, Kwiatkowski A, Leyson G, Kuzmina M et al (2017) Confined chemical and structural states at dislocations in Fe–9wt%Mn steels: a correlative TEM-atom probe study combined with multiscale modelling. *Acta Mater.* 124:305. <https://doi.org/10.1016/j.actamat.2016.11.013>
- [19] Kuzmina M, Herbig M, Ponge D, Sandlobes S, Raabe D (2015) Linear complexions: confined chemical and structural states at dislocations. *Science* 349:1080. <https://doi.org/10.1126/science.aab2633>
- [20] Raabe D, Herbig M, Sandlobes S et al (2014) Grain boundary segregation engineering in metallic alloys: a pathway to the design of interfaces. *Curr Opin Solid State Mater Sci* 18:253. <https://doi.org/10.1016/j.cossms.2014.06.002>
- [21] Linlin Li ZL, Kwiatkowski A, da Silva Z, Peng HZ, Gault B, Raabe D (2019) Segregation-driven grain boundary spinodal decomposition as a pathway for phase nucleation in a high-entropy alloy. *Acta Mater* 178:1. <https://doi.org/10.1016/j.actamat.2019.07.052>
- [22] Kwiatkowski DA, Da Silva Z, Peng G, Inden Y, Lu A, Breen BG, Raabe D (2018) Phase nucleation through confined spinodal fluctuations at crystal defects evidenced in Fe–Mn alloys. *Nat Commun* 9:1. <https://doi.org/10.1038/s41467-018-03591-4>
- [23] Li L, Li Z, da Silva AK et al (2019) Segregation-driven grain boundary spinodal decomposition as a pathway for phase nucleation in a high-entropy alloy. *Acta Mater* 178:1. <https://doi.org/10.1016/j.actamat.2019.07.052>
- [24] Kwiatkowski A, da Silva G, Inden AK, Ponge D, Gault B, Raabe D (2018) Competition between formation of carbides and reversed austenite during tempering of a medium-manganese steel studied by thermodynamic-kinetic simulations and atom probe tomography. *Acta Mater* 147:165. <https://doi.org/10.1016/j.actamat.2018.01.022>
- [25] Zhao JC, Notis MR (1998) Spinodal decomposition, ordering transformation, and discontinuous precipitation in a Cu–15Ni–8Sn alloy. *Acta Mater* 46:4203. [https://doi.org/10.1016/S1359-6454\(98\)00095-0](https://doi.org/10.1016/S1359-6454(98)00095-0)
- [26] Ramanarayan H, Abinandanan TA (2004) Grain boundary effects on spinodal decomposition: II Discontinuous microstructures. *Acta Mater* 52:921. <https://doi.org/10.1016/j.actamat.2003.10.028>
- [27] Feng B, Yokoi T, Kumamoto A, Yoshiya M, Ikuhara Y, Shibata N (2016) Atomically ordered solute segregation behaviour in an oxide grain boundary. *Nat Commun* 7:11079. <https://doi.org/10.1038/ncomms11079>
- [28] Lejček P (2013) Effect of solute interaction on interfacial segregation and grain boundary embrittlement in binary alloys. *J Mater Sci* 48:2574. <https://doi.org/10.1007/s10853-012-7048-0>
- [29] Hersent E, Marthinsen K, Nes E (2013) The effect of solute atoms on grain boundary migration: a solute pinning approach. *Metall Mater Trans A* 44:3364. <https://doi.org/10.1007/s11661-012-1552-3>
- [30] Furrer P, Gronsky R (1981) Grain boundary precipitation in aluminum alloys: effect of boundary structure. *Am Soc Met Metall Soc Aime* 12A:121. <https://doi.org/10.1007/BF02648516>
- [31] Hiroaki Kurishita SK (1985) Misorientation dependence of grain boundary. *Trans Jpn Inst Met* 26:332. <https://doi.org/10.2320/matertrans1960.26.332>
- [32] Oliveira MM, Soares PC, Bueno PR, Leite ER, Longo E, Varela JA (2003) Grain-boundary segregation and precipitates in La₂O₃ and Pr₂O₃ doped SnO₂-CoO-based varistors. *J Eur Ceram Soc* 23:1875. [https://doi.org/10.1016/s0955-2219\(02\)00445-4](https://doi.org/10.1016/s0955-2219(02)00445-4)
- [33] Das S, Mukherjee M, Pal TK (2015) Effect of grain boundary precipitation and δ -ferrite formation on surface defect of low nickel austenitic stainless steels. *Eng Fail Anal* 54:90. <https://doi.org/10.1016/j.engfailanal.2015.04.010>
- [34] Moskovkin P, Hou M (2003) Thermal evolution of cluster assembled Ni₃Al materials modelled at the atomic scale. *Eur Phys J D—At, Mol Opt Phys* 27:231. <https://doi.org/10.1140/epjd/e2003-00277-3>
- [35] Malik A, Odqvist J, Höglund L, Hertzman S, Ågren J (2017) Phase-Field modeling of sigma-phase precipitation in 25Cr₇Ni₄Mo duplex stainless steel. *Metall Mater Trans A* 48:4914. <https://doi.org/10.1007/s11661-017-4214-7>
- [36] Dong W, Wang Y, Yang K, Chen Z, Lu Y (2011) Phase field simulation of interatomic potentials for double phase competition during early stage precipitation. *Chin Sci Bull* 56:2055. <https://doi.org/10.1007/s11434-011-4407-1>
- [37] Faginas Lago N, Alberti M, Lombardi A, Pirani F (2016) A force field for acetone: the transition from small clusters to liquid phase investigated by molecular dynamics simulations. *Theor Chem Acc.* <https://doi.org/10.1007/s00214-016-1914-9>
- [38] El Mekkaoui N, Idrissi S, Mtougui S et al (2019) Monte Carlo study of the manganite oxide perovskite YMnO₃. *Appl Phys A.* <https://doi.org/10.1007/s00339-019-2880-6>
- [39] Turlo V, Rupert TJ (2020) Prediction of a wide variety of linear complexions in face centered cubic alloys. *Acta Mater* 185:129. <https://doi.org/10.1016/j.actamat.2019.11.069>
- [40] Turlo V, Rupert TJ (2019) Linear complexions: metastable phase formation and coexistence at dislocations. *Phys Rev Lett* 122:126102. <https://doi.org/10.1103/PhysRevLett.122.126102>

- [41] Dontsova E, Rottler J, Sinclair CW (2015) Solute segregation kinetics and dislocation depinning in a binary alloy. *Phys Rev B*. <https://doi.org/10.1103/PhysRevB.91.224103>
- [42] Dontsova E, Rottler J, Sinclair CW (2014) Solute-defect interactions in Al–Mg alloys from diffusive variational Gaussian calculations. *Phys Rev B*. <https://doi.org/10.1103/PhysRevB.90.174102>
- [43] Li J, Sarkar S, Cox WT, Lenosky TJ, Bitzek E, Wang Y (2011) Diffusive molecular dynamics and its application to nanoindentation and sintering. *Phys Rev B*. <https://doi.org/10.1103/PhysRevB.84.054103>
- [44] Greenwood M, Provatas N, Rottler J (2010) Free energy functionals for efficient phase field crystal modeling of structural phase transformations. *Phys Rev Lett* 105:045702. <https://doi.org/10.1103/PhysRevLett.105.045702>
- [45] Greenwood M, Ofori-Opoku N, Rottler J, Provatas N (2011) Modeling structural transformations in binary alloys with phase field crystals. *Phys Rev B*. <https://doi.org/10.1103/PhysRevB.84.064104>
- [46] Elder KR, Provatas N, Berry J, Stefanovic P, Grant M (2007) Phase-field crystal modeling and classical density functional theory of freezing. *Phys Rev B* 75:794. <https://doi.org/10.1103/PhysRevB.75.064107>
- [47] Huang ZF, Elder KR, Provatas N (2010) Phase-field-crystal dynamics for binary systems: derivation from dynamical density functional theory amplitude equation formalism and applications to alloy heterostructures. *Phys Rev E Stat Nonlinear Soft Matter Phys* 82:021605. <https://doi.org/10.1103/PhysRevE.82.021605>
- [48] Provatas N, Elder K (2010) *Phase-Field methods in materials science and engineering*. Wiley
- [49] Greenwood M, Rottler J, Provatas N (2011) Phase-field-crystal methodology for modeling of structural transformations. *Phys Rev E Stat Nonlinear Soft Matter Phys* 83:031601. <https://doi.org/10.1103/PhysRevE.83.031601>
- [50] Fallah V, Ofori-Opoku N, Stolle J, Provatas N, Esmaili S (2013) Simulation of early-stage clustering in ternary metal alloys using the phase-field crystal method. *Acta Mater* 61:3653. <https://doi.org/10.1016/j.actamat.2013.02.053>
- [51] Gránásy L, Tegze G, Tóth GI, Pusztai T (2011) Phase-field crystal modelling of crystal nucleation, heteroepitaxy and patterning. *Philos Mag* 91:123. <https://doi.org/10.1080/14786435.2010.487476>
- [52] Fallah V, Korinek A, Ofori-Opoku N, Provatas N, Esmaili S (2013) Atomistic investigation of clustering phenomenon in the Al–Cu system: three-dimensional phase-field crystal simulation and HRTEM/HRSTEM characterization. *Acta Mater* 61:6372. <https://doi.org/10.1016/j.actamat.2013.07.015>
- [53] Hu Y, Chen YQ, Li L, Hu HD, Zhu ZA (2016) Microstructure and properties of Al/Cu bimetal in liquid–solid compound casting process. *Trans Nonferr Met Soc China* 26:1555. [https://doi.org/10.1016/s1003-6326\(16\)64261-9](https://doi.org/10.1016/s1003-6326(16)64261-9)
- [54] Rosalie JM, Bourgeois L, Muddle BC (2012) Precipitation of the phase in Al–Cu–Ag alloys. *Light Metals*. Springer, pp 307–312
- [55] Brown JE, Smith GDW (1991) Atom probe studies of spinodal processes in duplex stainless steels and single and dual phase Fe–Cr–Ni alloys. *Surf Sci* 1(3):285–291. [https://doi.org/10.1016/0039-6028\(91\)90428-U](https://doi.org/10.1016/0039-6028(91)90428-U)
- [56] Danoix F, Auger P, Bostel A, Blavette D (1991) Atom probe characterization of isotropic spinodal decompositions: spatial convolutions and related bias. *Surf Sci* 246:A173. [https://doi.org/10.1016/0039-6028\(91\)90424-Q](https://doi.org/10.1016/0039-6028(91)90424-Q)
- [57] Müller M, Smith GDW, Gault B, Grovenor CRM (2012) Phase separation in thick InGaN layers—a quantitative, nanoscale study by pulsed laser atom probe tomography. *Acta Mater* 60:4277. <https://doi.org/10.1016/j.actamat.2012.04.030>
- [58] Knutsson A, Schramm IC, Asp Gronhagen K, Mucklich F, Oden M (2013) Surface directed spinodal decomposition at TiAlN/TiN interfaces. *J Appl Phys* 113:114305. <https://doi.org/10.1063/1.4795155>
- [59] Cantwell PR, Tang M, Dillon SJ, Luo J, Rohrer GS, Harmer MP (2014) Grain boundary complexions. *Acta Mater* 62:1. <https://doi.org/10.1016/j.actamat.2013.07.037>
- [60] Meiners T, Frolov T, Rudd RE, Dehm G, Liebscher CH (2020) Observations of grain-boundary phase transformations in an elemental metal. *Nature* 579:375. <https://doi.org/10.1038/s41586-020-2082-6>
- [61] Sahu S, Patel SK, Shekhar S (2020) The effect of grain boundary structure on chromium carbide precipitation in Alloy 600. *Mater Chem Phys*. <https://doi.org/10.1016/j.materchemphys.2020.124145>
- [62] Bjorge R, Marioara CD, Andersen SJ, Holmestad R (2010) Germanium network connecting precipitates in an Mg–rich Al–Mg–Ge alloy. *J Electron Microsc*. <https://doi.org/10.1093/jmicro/dfq040>
- [63] Kishida K, Yokobayashi H, Inui H (2017) A formation criterion for Order-Disorder (OD) phases of the long-period stacking order (LPSO)-type in Mg–Al–RE (rare earth) ternary systems. *Sci Rep*. <https://doi.org/10.1038/s41598-017-12506-0>
- [64] Jin S, Ngai T, Li L, Jia S, Zhai T, Ke D (2018) Aging response and precipitation behavior after 5% pre-deformation of an Al–Mg–Si–Cu alloy. *Materials*. <https://doi.org/10.3390/ma11081422>

- [65] Maeda T, Kaneko K, Namba T et al (2018) Structural and compositional study of precipitates in under-aged Cu-added Al–Mg–Si alloy. *Sci Rep.* <https://doi.org/10.1038/s41598-018-35134-8>

Publisher's Note Springer Nature remains neutral with regard to jurisdictional claims in published maps and institutional affiliations.